KSCE Journal of Civil Engineering (2019) 23(9):3793-3806

DOI 10.1007/s12205-019-0786-7

Geotechnical Engineering

pISSN 1226-7988, eISSN 1976-3808
www.springer.com/12205

Stress Distribution and Failure Characteristics for Workface Floor of a Tilted Coal Seam

Jian Sun*, Lianguo Wang, and Guangming Zhao*****

Received April 21, 2018/Accepted June 30, 2019/Published Online August 6, 2019

Abstract

A mechanical model for the tilted workface floor along the tilted direction of coal seam was proposed. Stress expressions of an arbitrary point inside the tilted workface floor were deduced. Calculation formula for the maximum failure depth of the lateral floor strata of the tilted workface was also deduced. Based on the Mohr-Coulomb yield criterion, the tilted workface floor's stress distribution, and failure depth and shape were simulated by using FLAC^{3D} software for different coal seam's dip angles, buried depths, and workface widths. Results show that the concentration coefficient, the peak value and the distance between the peak position of the lateral abutment pressure and the roadway on both sides of the tilted workface decreases with the increases in coal seam's dip angle. The vertical stress isoclines present a "spoon-shaped" distribution along the tilted direction of workface. Both sides of the workface form "bubble-shaped" distribution shear stress and its peak value increases first and then decreases with the increases in coal seam's dip angle and reaches maximum at 30°–35°. The tilted workface floor's plastic failure zone presents a "spoon-shaped" distribution along the tilted direction of workface, which is large on the lower side and small on the upper side. The plastic zone's failure depth increases first and then decreases with the increases in the dip angle of coal seam and reaches maximum at 30°.

Keywords: *tilted coal seam, workface floor, stress distribution, failure characteristics, failure depth, failure shape*

1. Introduction

The roof and floor strata of workface are in a state of stress balance before mining, and the stresses on roof and floor strata of workface are redistributed after mining. Formation of stress concentration and reduction area can possibly result in the deformation and failure of stope surrounding rock (Jiang *et al*., 2011; Lu *et al*., 2014). Therefore, studying the stress distribution of workface floor and mining failure depth, shape and its influence on realizing the safe mining above confined aquifer is necessary, which can determine the proper location of floor roadway and the mining influence of upper coal seam on lower coal seam (Xiao *et al*., 2010; Zhang *et al*., 2012; Zhao *et al*., 2015).

Liu *et al.* (2016) analyzed the stress distribution of workface floor and the roadway position in the close distance coal seams. Liu *et al.* (2019; 2017) studied the evolution law of stress and failure characteristics of the mining workface floor above confined aquifer, and analyzed the evolution characteristics of water inrush from workface floor. Lu *et al.* (2015) numerical simulated the fracture evolution and the water flow in workface floor above confined aquifer. Zhang and Meng (2019), and Zhang *et al.* (2017) studied the floor failure of mining workface above confined aquifer, and analyzed the evolutionary process of water inrush from floor by the method of experimental simulation. Yin *et al.* (2016) monitored the stress evolution law of workface floor with time and space during mining. Tan *et al.* (2010) investigated the failure zone of workface floor in mining of the close distance coal seams. Zhu *et al.* (2014) studied the workface floor's deformation and failure characteristics due to coal seam mining. Cheng *et al.* (2015) studied the control method of rock burst in floor roadway that driven along the goaf in a thick coal seam with a large dip angle.

Otherwise, based on the elastic mechanics theory of the space semi-infinite body, many scholars studied the mining workface floor's stress distribution and failure depth by combining the Mohr–Coulomb yield criterion and the numerical simulation method. Wang *et al.* (2013) built a spatial semi-infinite body model that allows for the advanced and inclined directions of workface and derived the iterative formula of vertical stress of stope floor. And they also calculated the workface floor's maximum failure depth by combining Mohr–Coulomb yield criterion and

*Associate Professor, School of Energy and Safety, Anhui University of Science and Technology, Huainan 232001, China (Corresponding Author, E-mail: sj323@cumt.edu.cn)

**Professor, State Key Laboratory For Geomechanics and Deep Undergroud Engineering, China University of Mining and Technology, Xuzhou 221116, China (E-mail: lgwang@cumt.edu.cn)

***Professor, School of Energy and Safety, Anhui University of Science and Technology, Huainan 232001, China (E-mail: guangmingzhao@163.com)

compared the failure depth with the micro-seismic monitoring results. According to the distribution law of the advance abutment pressure in front of the workface, Meng *et al.* (2010) built an elastic mechanics model of stress calculation with an arbitrary point in stope floor, provided evidence for determining the failure of workface floor using the Mohr–Coulomb yield criterion, and analyzed the stress distribution and failure mechanism of the 1028 workface floor in Suntong Mine. Li *et al.* (2015) studied the floor failure law using the finite element method with Zhaogu Mine II as the engineering background, measured the floor failure depths of different mining heights using the mine symmetrical quadrupole electrical profiling method, and performed multivariate statistics regression analysis of mining floor failure influential factors and failure depth using the Spass software. Zhang *et al.* (2013) took the deep mining of a full-mechanized workface as the engineering background, confirmed the deformation and failure of workface floor with different buried depths of coal seam, and discussed the basic laws of deformation and failure of workface floor of a thick coal seam with considerable mining depth by combining the numerical simulation results. Feng *et al.* (2015) decomposed the stress field of stope floor into initial and excavation stress fields, built the floor strata mechanics model that allows for the abutment pressure of the lateral wall, performed the analytic calculation of the floor stress and displacement fields using the integral transformation method, and determined the workface floor's plastic failure depth with the Mohr–Coulomb yield criterion. Liu *et al.* (2015; 2018) considered several factors, such as the inclined length of workface, mining thickness, mining depth and floor strata mechanics parameters, and water pressure, simulated the effect of such factors on the mining workface floor's failure depth by using FLAC software, and studied the sensibility of the main controlling factors that affect the floor failure depth.

China is rich in coal resources, and its existing coal seam conditions are quite diversified. Furthermore, the hydrogeology is complicated, with significant changes in coal seam's dip angle. In addition to the approximately horizontal coal seam with relatively small dip angle, numerous tilted coal seams with relatively large dip angles exist (Sun, 2011; Sun and Wang, 2014; Sun *et al.*, 2011). The deformation and failure of surrounding rock of the tilted coal seam workface is quite different from that of the horizontal and approximately horizontal coal seam. In the past, scholars only studied the deformation and failure characteristics of workface floor after mining of the horizontal and approximately horizontal coal seam, and research on the stress distribution, failure depth, and failure shape and scope of workface floor of a tilted coal seam is limited. According to the literature review of Sun (2011), Liu *et al.* (2017) built the mechanical model along the tilted direction of workface floor for calculating the failure depth of mining workface floor based on the elastic mechanics theory of the semi-infinite body by designing an orthogonal test scheme and performed a simulation analysis of the sensibility of the main controlling factors that affect the failure depth of workface floor. Chen *et al.* (2016) detected the failure depth of the full-mechanized mining workface floor in a tilted super-thick coal seam with considerable mining depth using the segmental water injection device, the borehole TV system, and the geological radar. And they also conducted a numerical simulation of the number of floor fissures, borehole depth, and failure width and number before and after mining, including floor stress variation and plastic zone characteristics.

Owing to the inclination of coal seam, the stress distribution (vertical stress and shearing stress) and the failure characteristics (failure depth and failure shape) of workface floor are quite different from that of the horizontal and approximately horizontal workface floor of coal seam, as they are more susceptible to factors such as the coal seam's dip angle, the workface width, and the buried depth, and the relevant studies should be extended. Therefore, in this study, a mechanical model for the tilted workface floor along the tilted direction of coal seam with longwall mining was proposed according to the occurrence characteristics of the tilted coal seam. By adopting the elastic mechanics theory and combining the Mohr–Coulomb yield criterion, the stress expression of an arbitrary point inside the tilted workface floor along the tilted direction of coal seam and the calculation formula for the maximum failure depth were derived. Moreover, a three-dimensional numerical model for the tilted workface with longwall mining was built by using FLAC^{3D} software to simulate and analyze the laws of the stress distribution, and the failure depth and shape of a tilted workface floor along the tilted direction of coal seam, which changes with the dip angle, buried depth, and workface width of coal seam.

2. Mechanical Analysis of the Stress Distribution and Failure Characteristics for the Tilted Workface Floor

2.1 Mechanical Model for the Tilted Workface Floor

After mining, whether the horizontal or approximately horizontal or tilted coal seam, an advance abutment pressure is formed in

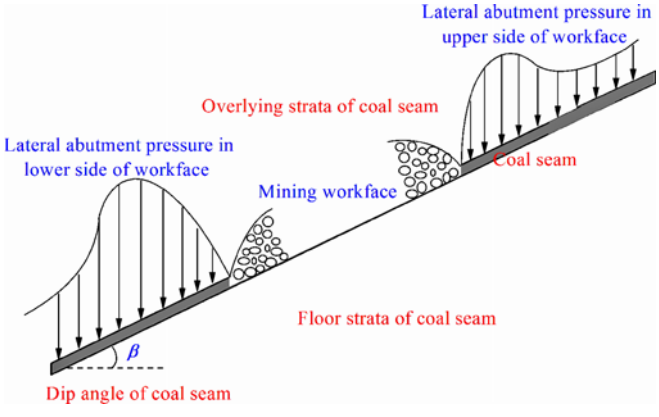

Fig. 1. The Lateral Abutment Pressure Distribution of the Tilted Workface along the Tilted Direction

front of the workface, and two lateral abutment pressures are formed on both sides of the workface. The overlying strata stress is transferred to the stope surrounding rock, thereby resulting in the deformation and failure of the stope surrounding rock. For the workface of a tilted coal seam, the abutment pressure distribution in surrounding rock of the tilted workface has its own distribution characteristics in addition to those of the horizontal and approximately horizontal workface. Fig. 1 shows the schematic of the lateral abutment pressure distribution of a tilted workface along the tilted direction of coal seam in longwall mining. The peak values of the lateral abutment pressure and the distribution range and their distance from both sides of the roadway coal walls, which are the distribution characteristics of the lateral abutment pressure of a tilted workface, are quite different because the buried depths of both sides of the roadways of the tilted workface are different.

The tilted workface floor strata along the tilted direction of coal seam was predigested as a spatial semi-infinite body to investigate the tilted workface floor's stress distribution and failure characteristics along the tilted direction of coal seam in longwall mining. In addition, the lateral abutment pressure of workface in Fig. 1 was decomposed into transverse and longitudinal force perpendicular and parallel to the workface floor, respectively, and was simplified as a linear load and loaded to the spatial semi-infinite body. The mechanical model for the tilted workface floor along the tilted direction of coal seam in longwall mining was built, as shown in Fig. 2. The established rectangular coordinate system was also described in Fig. 2, where the coal seam's dip angle is β, the buried depth at workface crossheading is H, the height of caving zone is H_m, and the bulk density of floor strata is γ.

In Fig. 2, the vertical projection points of the linearly distributed loads' inflection point on x-axis are o, a, b, c, d, e, f, and g, and the s_1, s_2, s_3, s_4, s_5, s_6, and s_7 are the distances between the vertical projection points of two adjacent inflection points. The k_1, k_2, k_3, and k_4 are the concentration factors of the lateral abutment pressure and they satisfy $k_1 > k_2 > 1 > k_3 > k_4$. The areas of ①②③④⑤⑥⑦ are the simplified transverse components of the abutment pressures at the direction perpendicular to the workface floor (the transverse force causes compression failure to floor strata), and the areas of ⑧⑨⑩⑪⑫⑬⑭ are the longitudinal components of the abutment pressures at the direction parallel to the workface floor (the longitudinal force produces a tilted bottom shear force along the workface floor, which results in the slippage of floor strata and shear failure). The transverse load ④ that the caving zone produces on the workface floor is $\gamma H_m \cos\beta$, and the longitudinal load ⑪ is $\gamma H_m \sin\beta$. For the transverse load, the $k_4\gamma H\cos\beta$ of point o at the upper edge of workface linearly increased to the $k_2\gamma(H + x_a\sin\beta)\cos\beta$ of point a and then decreased to the primary rock stress $\gamma(H + x_b\sin\beta)\cos\beta$ of point b, and the $k_3\gamma(H + x_d\sin\beta)\cos\beta$ of point d at the lower edge of workface linearly increased to the $k_1\gamma(H + x_e\sin\beta)\cos\beta$ of point e and then decreased to the primary rock stress $\gamma(H + x_f\sin\beta)\cos\beta$ of point f. For the longitudinal load, the $k_4\gamma H\sin\beta$ of point o at the upper edge of workface linearly increased to the $k_2\gamma(H + x_a\sin\beta)\sin\beta$ of point a and then decreased to the primary rock stress $\gamma(H + x_b\sin\beta)\sin\beta$ of point b, and the $k_3\gamma(H + x_d\sin\beta)\sin\beta$ of point d at the lower edge of workface increased to the $k_1\gamma(H + x_e\sin\beta)\sin\beta$ of point e and then decreased to the primary rock stress $\gamma(H + x_f\sin\beta)\sin\beta$ of point f.

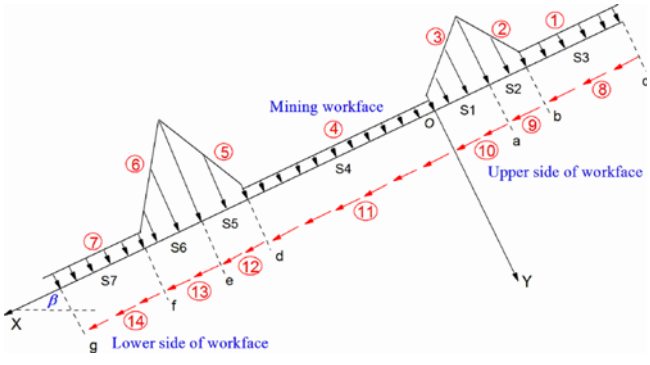

Fig. 2. Mechanical Model for the Tilted Workface Floor along the Tilted Direction of Coal Seam

2.2 Stress Distribution for the Tilted Workface Floor

Based on the elastic mechanics theory of the homogeneous isotropic spatial semi-infinite body (Timoshenko and Woinowsky-Krieger, 1959), the expressions of stresses σ_x, σ_y, and τ_{xy} of arbitrary points inside the tilted workface floor along the tilted direction of coal seam can be obtained, as shown in Eqs. (1), (2), and (3), respectively.

$$
\begin{aligned}
\sigma_x &= \sigma_{x1} + \sigma_{x2} + \sigma_{x3} + \sigma_{x4} + \sigma_{x5} + \sigma_{x6} + \sigma_{x7} + \sigma_{x8} + \sigma_{x9} + \sigma_{x10} + \sigma_{x11} \\
&\quad + \sigma_{x12} + \sigma_{x13} + \sigma_{x14} \\
&= \frac{2}{\pi}\int_{-(s_1+s_2)}^{(s_1+s_2+s_3)} \frac{(q+\xi p)(x-\xi)^2 y}{\left[(x-\xi)^2+y^2\right]^2}d\xi + \frac{2}{\pi}\int_{-(s_1+s_2)}^{s_1} \frac{(A+\xi B)(x-\xi)^2 y}{\left[(x-\xi)^2+y^2\right]^2}d\xi \\
&\quad + \frac{2}{\pi}\int_{-s_1}^{0} \frac{(C+\xi D)(x-\xi)^2 y}{\left[(x-\xi)^2+y^2\right]^2}d\xi + \frac{2}{\pi}\int_{0}^{s_4} \frac{\gamma H_m \cos\beta (x-\xi)^2 y}{\left[(x-\xi)^2+y^2\right]^2}d\xi \\
&\quad + \frac{2}{\pi}\int_{s_4}^{s_4+s_5} \frac{(E+\xi F)(x-\xi)^2 y}{\left[(x-\xi)^2+y^2\right]^2}d\xi + \frac{2}{\pi}\int_{s_4+s_5}^{s_4+s_5+s_6} \frac{(G+\xi I)(x-\xi)^2 y}{\left[(x-\xi)^2+y^2\right]^2}d\xi \\
&\quad + \frac{2}{\pi}\int_{s_4+s_5+s_6}^{s_4+s_5+s_6+s_7} \frac{(q+\xi p)(x-\xi)^2 y}{\left[(x-\xi)^2+y^2\right]^2}d\xi + \frac{2}{\pi}\int_{-(s_1+s_2)}^{(s_1+s_2+s_3)} \frac{(q+\xi p)\tan\beta (x-\xi)^3}{\left[(x-\xi)^2+y^2\right]^2}d\xi \\
&\quad + \frac{2}{\pi}\int_{-(s_1+s_2)}^{s_1} \frac{(A+\xi B)\tan\beta (x-\xi)^3}{\left[(x-\xi)^2+y^2\right]^2}d\xi + \frac{2}{\pi}\int_{-s_1}^{0} \frac{(C+\xi D)\tan\beta (x-\xi)^3}{\left[(x-\xi)^2+y^2\right]^2}d\xi \\
&\quad + \frac{2}{\pi}\int_{0}^{s_4} \frac{\gamma H_m \sin\beta (x-\xi)^3}{\left[(x-\xi)^2+y^2\right]^2}d\xi + \frac{2}{\pi}\int_{s_4}^{s_4+s_5} \frac{(E+\xi F)\tan\beta (x-\xi)^3}{\left[(x-\xi)^2+y^2\right]^2}d\xi \\
&\quad + \frac{2}{\pi}\int_{s_4+s_5}^{s_4+s_5+s_6} \frac{(G+\xi I)\tan\beta (x-\xi)^3}{\left[(x-\xi)^2+y^2\right]^2}d\xi + \frac{2}{\pi}\int_{s_4+s_5+s_6}^{s_4+s_5+s_6+s_7} \frac{(q+\xi p)\tan\beta (x-\xi)^3}{\left[(x-\xi)^2+y^2\right]^2}d\xi
\end{aligned}
\tag{1}
$$

$$\sigma_y=\sigma_{y1}+\sigma_{y2}+\sigma_{y3}+\sigma_{y4}+\sigma_{y5}+\sigma_{y6}+\sigma_{y7}+\sigma_{y8}+\sigma_{y9}+\sigma_{y10}+\sigma_{y11}+\sigma_{y12}+\sigma_{y13}+\sigma_{y14}$$
$$=\frac{2}{\pi}\int_{(s_1+s_2+s_3)}^{(s_1+s_2)}\frac{(q+\xi p)y^3}{\left[(x-\xi)^2+y^2\right]^2}d\xi+\frac{2}{\pi}\int_{(s_1+s_2)}^{s_1}\frac{(A+\xi B)y^3}{\left[(x-\xi)^2+y^2\right]^2}d\xi$$
$$+\frac{2}{\pi}\int_{s_1}^{0}\frac{(C+\xi D)y^3}{\left[(x-\xi)^2+y^2\right]^2}d\xi+\frac{2}{\pi}\int_{0}^{s_4}\frac{\gamma H_m\cos\beta y^3}{\left[(x-\xi)^2+y^2\right]^2}d\xi$$
$$+\frac{2}{\pi}\int_{s_4}^{s_4+s_5}\frac{(E+\xi F)y^3}{\left[(x-\xi)^2+y^2\right]^2}d\xi+\frac{2}{\pi}\int_{s_4+s_5}^{s_4+s_5+s_6}\frac{(G+\xi I)y^3}{\left[(x-\xi)^2+y^2\right]^2}d\xi$$
$$+\frac{2}{\pi}\int_{s_4+s_5+s_6}^{s_4+s_5+s_6+s_7}\frac{(q+\xi p)y^3}{\left[(x-\xi)^2+y^2\right]^2}d\xi+\frac{2}{\pi}\int_{(s_1+s_2+s_3)}^{(s_1+s_2)}\frac{(q+\xi p)\tan\beta(x-\xi)y^2}{\left[(x-\xi)^2+y^2\right]^2}d\xi$$
$$+\frac{2}{\pi}\int_{(s_1+s_2)}^{s_1}\frac{(A+\xi B)\tan\beta(x-\xi)y^2}{\left[(x-\xi)^2+y^2\right]^2}d\xi+\frac{2}{\pi}\int_{s_1}^{0}\frac{(C+\xi D)\tan\beta(x-\xi)y^2}{\left[(x-\xi)^2+y^2\right]^2}d\xi$$
$$+\frac{2}{\pi}\int_{0}^{s_4}\frac{\gamma H_m\sin\beta(x-\xi)y^2}{\left[(x-\xi)^2+y^2\right]^2}d\xi+\frac{2}{\pi}\int_{s_4}^{s_4+s_5}\frac{(E+\xi F)\tan\beta(x-\xi)y^2}{\left[(x-\xi)^2+y^2\right]^2}d\xi$$
$$+\frac{2}{\pi}\int_{s_4+s_5}^{s_4+s_5+s_6}\frac{(G+\xi I)\tan\beta(x-\xi)y^2}{\left[(x-\xi)^2+y^2\right]^2}d\xi+\frac{2}{\pi}\int_{s_4+s_5+s_6}^{s_4+s_5+s_6+s_7}\frac{(q+\xi p)\tan\beta(x-\xi)y^2}{\left[(x-\xi)^2+y^2\right]^2}d\xi \tag{2}$$

$$\tau_{xy}=\tau_{xy1}+\tau_{xy2}+\tau_{xy3}+\tau_{xy4}+\tau_{xy5}+\tau_{xy6}+\tau_{xy7}+\tau_{xy8}+\tau_{xy9}+\tau_{xy10}+\tau_{xy11}+\tau_{xy12}+\tau_{xy13}+\tau_{xy14}$$
$$=\frac{2}{\pi}\int_{(s_1+s_2+s_3)}^{(s_1+s_2)}\frac{(q+\xi p)(x-\xi)y^2}{\left[(x-\xi)^2+y^2\right]^2}d\xi+\frac{2}{\pi}\int_{(s_1+s_2)}^{s_1}\frac{(A+\xi B)(x-\xi)y^2}{\left[(x-\xi)^2+y^2\right]^2}d\xi$$
$$+\frac{2}{\pi}\int_{s_1}^{0}\frac{(C+\xi D)(x-\xi)y^2}{\left[(x-\xi)^2+y^2\right]^2}d\xi+\frac{2}{\pi}\int_{0}^{s_4}\frac{\gamma H_m\cos\beta(x-\xi)y^2}{\left[(x-\xi)^2+y^2\right]^2}d\xi$$
$$+\frac{2}{\pi}\int_{s_4}^{s_4+s_5}\frac{(E+\xi F)(x-\xi)y^2}{\left[(x-\xi)^2+y^2\right]^2}d\xi+\frac{2}{\pi}\int_{s_4+s_5}^{s_4+s_5+s_6}\frac{(G+\xi I)(x-\xi)y^2}{\left[(x-\xi)^2+y^2\right]^2}d\xi$$
$$+\frac{2}{\pi}\int_{s_4+s_5+s_6}^{s_4+s_5+s_6+s_7}\frac{(q+\xi p)(x-\xi)y^2}{\left[(x-\xi)^2+y^2\right]^2}d\xi+\frac{2}{\pi}\int_{(s_1+s_2+s_3)}^{(s_1+s_2)}\frac{(q+\xi p)\tan\beta(x-\xi)^2y}{\left[(x-\xi)^2+y^2\right]^2}d\xi$$
$$+\frac{2}{\pi}\int_{(s_1+s_2)}^{s_1}\frac{(A+\xi B)\tan\beta(x-\xi)^2y}{\left[(x-\xi)^2+y^2\right]^2}d\xi+\frac{2}{\pi}\int_{s_1}^{0}\frac{(C+\xi D)\tan\beta(x-\xi)^2y}{\left[(x-\xi)^2+y^2\right]^2}d\xi$$
$$+\frac{2}{\pi}\int_{0}^{s_4}\frac{\gamma H_m\sin\beta(x-\xi)^2y}{\left[(x-\xi)^2+y^2\right]^2}d\xi+\frac{2}{\pi}\int_{s_4}^{s_4+s_5}\frac{(E+\xi F)\tan\beta(x-\xi)^2y}{\left[(x-\xi)^2+y^2\right]^2}d\xi+$$
$$\frac{2}{\pi}\int_{s_4+s_5}^{s_4+s_5+s_6}\frac{(G+\xi I)\tan\beta(x-\xi)^2y}{\left[(x-\xi)^2+y^2\right]^2}d\xi+\frac{2}{\pi}\int_{s_4+s_5+s_6}^{s_4+s_5+s_6+s_7}\frac{(q+\xi p)\tan\beta(x-\xi)^2y}{\left[(x-\xi)^2+y^2\right]^2}d\xi \tag{3}$$

where ξ is the variable of integration in Eqs. (1), (2), and (3), and the other integration parameters are as follows:

$$q=\gamma H\cos\beta,\quad p=\gamma\sin\beta\cos\beta$$
$$A=\frac{(k_2s_1+k_2s_2-s_1)q-(k_2s_1-s_1)(s_1+s_2)p}{s_2}$$
$$B=\frac{(k_1-1)q-(k_2s_1-s_1-s_2)p}{s_2},\quad C=k_4q$$
$$D=\frac{(k_4-k_2)q+k_2s_1p}{s_1}$$
$$E=\frac{(k_3s_5-k_1s_4+k_3s_4)q+(k_3s_4s_5-k_1s_4s_4-k_1s_4s_5+k_3s_4s_4)p}{s_5}$$
$$F=\frac{(k_1-k_3)q+(k_1s_4+k_1s_5-k_3s_4)p}{s_5}$$
$$G=k_1q+k_1(s_4+s_5)p-\frac{(1-k_1)q+(s_4+s_5+s_6-k_1s_4-k_1s_5)p}{s_6}(s_4+s_5)$$
$$I=\frac{(1-k_1)q+(s_4+s_5+s_6-k_1s_4-k_1s_5)p}{s_6} \tag{4}$$

For example, H = 500 m, H_m = 15 m, γ = 24 kN/m^3, k_1 = 3.0, k_2 = 2.5, k_3 = 0.2, k_4 = 0.1, $s_1 = s_2 = s_5 = s_6$ = 6 m, $s_3 = s_7$ = 12 m, and s_4 = 120 m. Figs. 3(a), 3(b), 3(c), 3(d), and 3(e) show the isoclines of vertical stress σ_y of the tilted workface floor along the tilted direction of coal seam when coal seam's dip angles are 0°, 20°, 30°, 40°, and 50°, respectively. The value in Fig. 3 is the specific value with the primary rock stress near the workface.

Figure 3 shows that the contour lines of the vertical stress of workface floor along the tilted direction of coal seam are symmetrically and asymmetrically distributed for the horizontal and the tilted coal seam, respectively. Moreover, the contour lines of vertical stresses inside the workface floor strata display a "spoon-shaped" distribution form for the tilted workface floor, that is, they are large in the lower side and small in the upper side. For the horizontal or the tilted coal seam, the contour lines of vertical stresses below coal bodies on both sides of the workface display a "bubble-shaped" distribution oblique to the coal body. The obliqueness degree to the coal body increases with the increases in coal seam's dip angle. Moreover, the lower obliqueness degree of contour line of the vertical stress to the coal body is larger and more evident than that of upper obliqueness degree.

2.3 Failure Depth for the Lateral Floor of the Tilted Workface

After mining of a tilted coal seam, the lateral abutment pressure (as shown in Fig. 1) is produced on both sides of the workface. The lateral abutment pressure is decomposed into q_1, which is a transverse load perpendicular to the workface floor strata, and q_2, which is a longitudinal load parallel to the workface floor strata. Both loads are simplified as equivalent uniformly distributed loads, as described in Fig. 4.

Based on the elastic mechanics theory of the homogeneous isotropic spatial semi-infinite body, the stress expression for an arbitrary point inside the workface floor strata below the lateral coal pillar of a tilted workface can be obtained, as shown in Eq. (5).

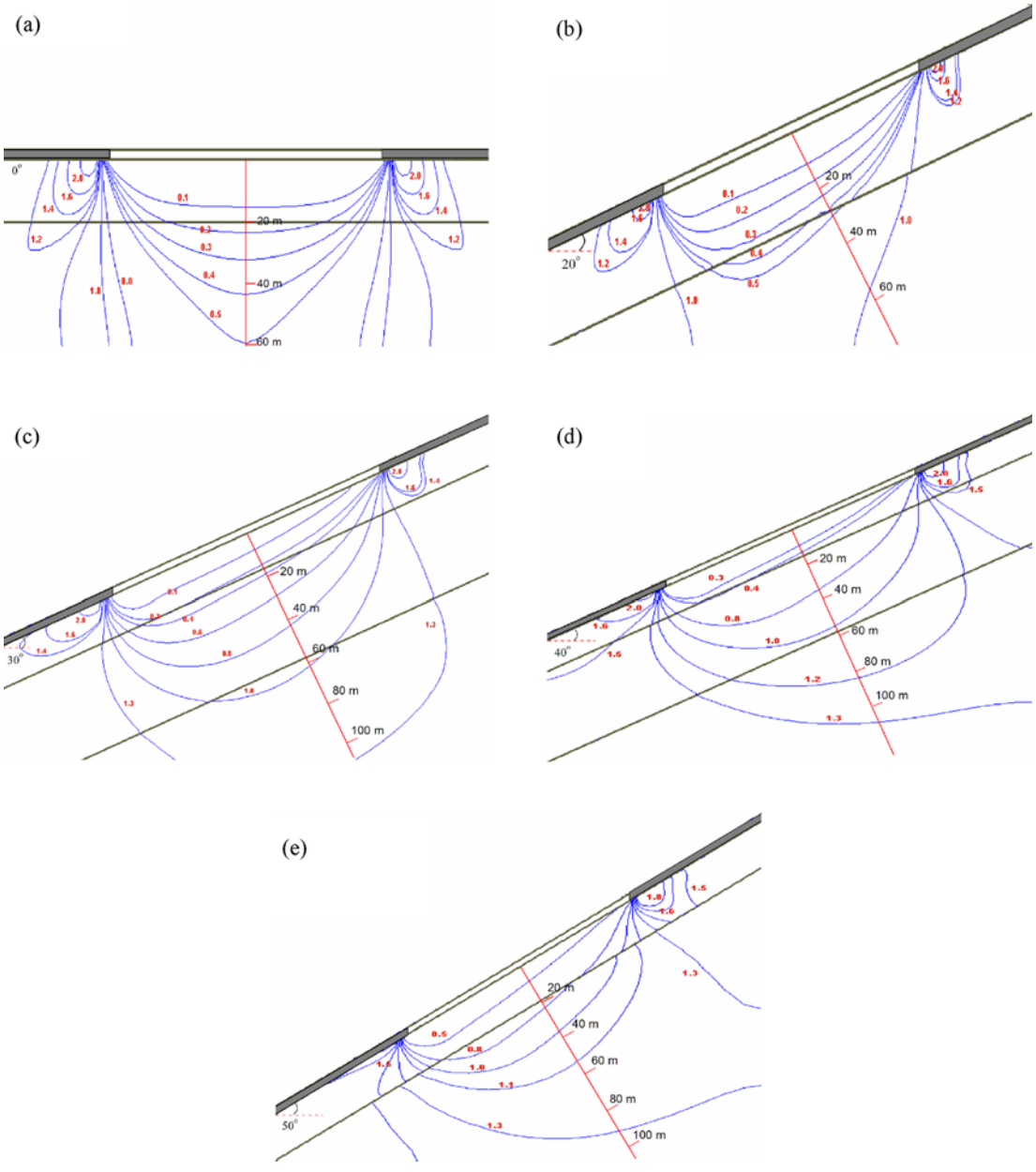

Fig. 3. Isoclines of Vertical Stress of the Tilted Workface Floor along the Tilted Direction for Different Dip Angles: (a) 0°, (b) 20°, (c) 30°, (d) 40°, (e) 50°

$$\left.\begin{aligned}
\sigma_x &= \frac{q_1}{\pi}\left[-\sin(\theta_2-\theta_1)\cos(\theta_2+\theta_1)+\theta_2-\theta_1\right] \\
&\quad+\frac{q_2}{\pi}\left[-\sin(\theta_2-\theta_1)\sin(\theta_2+\theta_1)+2\ln\frac{\cos\theta_1}{\cos\theta_2}\right] \\
\sigma_y &= \frac{q_1}{\pi}\left[\sin(\theta_2-\theta_1)\cos(\theta_2+\theta_1)+\theta_2-\theta_1\right] \\
&\quad+\frac{q_2}{\pi}\left[\sin(\theta_2-\theta_1)\sin(\theta_2+\theta_1)\right] \\
\tau_{xy} &= \frac{q_1}{\pi}\left[\sin(\theta_2-\theta_1)\sin(\theta_2+\theta_1)+\theta_2-\theta_1\right] \\
&\quad+\frac{q_2}{\pi}\left[-\sin(\theta_2-\theta_1)\cos(\theta_2+\theta_1)+\theta_2-\theta_1\right]
\end{aligned}\right\} \quad (5)$$

Equation (5) is substituted into the calculation formula of the principal stress, and the gravity stress ($\gamma y/\cos\beta$) of the lateral floor strata of a tilted workface is considered. Without affecting the computational accuracy, the logarithm part in σ_x of Eq. (5) is omitted. The principal stress of an arbitrary point inside the workface floor strata below the lateral coal pillar of a tilted workface can then be obtained, in which $\theta=\theta_2-\theta_1$.

$$\begin{aligned}
\sigma_1,\ \sigma_3 &= \frac{\sigma_x+\sigma_y}{2}\pm\sqrt{\left(\frac{\sigma_x-\sigma_y}{2}\right)^2+\left(\tau_{xy}\right)^2} \\
&= \frac{q_1}{\pi}\theta\pm\frac{1}{\pi}\left(\sqrt{q_1^2+q_2^2}\sin\theta+q_2\theta\right)+\frac{\gamma y}{\cos\beta}
\end{aligned} \quad (6)$$

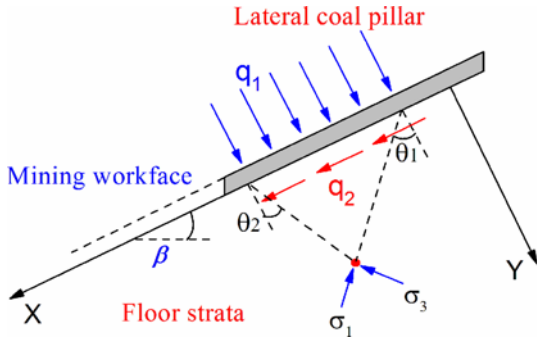

Fig. 4. Mechanical Model for the Lateral Floor of the Tilted Workface with Uniformly Distributed Load

When an arbitrary point of the workface floor strata affected by the lateral abutment pressure of workface is transiting from elastic to plastic state, the plastic deformation failure occurs at this point. The principal stress of this point must satisfy the limit equilibrium conditions. By adopting the Mohr–Coulomb yield criterion, that is, Eq. (7), the lateral abutment pressure $k\gamma H$ is decomposed into the transverse load q_1 perpendicular to the workface floor strata and the shear force q_2 parallel to the workface floor strata and replaced with equivalent uniformly distributed loads, namely, $q_1 = n\gamma H\cos\beta$ and $q_2 = n\gamma H\sin\beta$, in which $n = (k + 1)/2$, k is the concentration factor of the lateral abutment pressure of workface. Eq. (8) can be obtained as follows:

$$\frac{1}{2}(\sigma_1 - \sigma_3) = C\cos\varphi + \frac{1}{2}(\sigma_1 + \sigma_3)\sin\varphi \tag{7}$$

where C and φ are the tilted workface floor strata's cohesion and internal friction angle, respectively.

$$y = \frac{(k+1)H\cos\beta}{2\pi}\left[\frac{\sin\theta}{\sin\varphi} + \theta\left(\frac{\sin\beta}{\sin\varphi} - \cos\beta\right)\right] - \frac{C\cos\beta}{\gamma\tan\varphi} - \frac{m}{(\lambda - 1)} \tag{8}$$

where m is the mined coal seam's thickness, and the λ is the caving zone's bulking coefficient.

Let $dy/d\theta = 0$, $\theta = \arccos(\cos\beta\sin\varphi - \sin\beta)$. Then, the normal maximum failure depth h_0 of floor strata below the lateral coal pillar of a tilted workface can be obtained as shown in Eq. (9), in which $\phi = \arccos(\cos\beta\sin\varphi - \sin\beta)$.

$$h_0 = \frac{(k+1)H\cos\beta}{2\pi}\left[\frac{\sin\phi}{\sin\varphi} + \phi\left(\frac{\sin\beta}{\sin\varphi} - \cos\beta\right)\right] - \frac{C\cos\beta}{\gamma\tan\varphi} - \frac{m}{(\lambda - 1)} \tag{9}$$

Equation (9) indicates that the maximum failure depth of floor strata below the lateral coal body of a tilted workface increases with the increases in the lateral abutment pressure coefficient k of workface. The maximum failure depth increases as the buried depth increases and initially increases and then decreases as the dip angle increases.

When coal seam's dip angle is $\beta = 0°$, and $\phi = \pi/2 - \varphi$, Eq. (9) can be simplified as

$$h = \frac{(k+1)H}{2\pi}\left[\cot\varphi - \frac{\pi}{2} + \varphi\right] - \frac{C}{\gamma\tan\varphi} - H_m \tag{10}$$

Equation (10) is the calculation formula for the maximum failure depth of workface floor of a horizontal coal seam with the dip angle of 0°, which was derived by Zhang *et al.* (1997) using the elastic mechanics theory.

3. Numerical Analysis of the Stress Distribution and Failure Characteristics for the Tilted Workface Floor

3.1 Numerical Model for the Tilted Workface of Coal Seam

According to the engineering background of the tilted coal seam in longwall mining, a three-dimensional numerical calculation model for the tilted workface of coal seam in longwall mining was built, as shown in Fig. 5. The x and y are the tilted direction and advanced direction of workface, respectively. The coal seam's dip angle is β, the buried depth at the crossheading on workface is 500 m, the coal seam's thickness is 3 m, the workface width is 120 m, the horizontal width of coal pillar on both sides of the workface is 40 m, and the length of workface at the advanced direction is 200 m. A step by step excavation is adopted for the model, starting from y = 40 m with full-seam mining to y = 120 m and advancing at 15-m

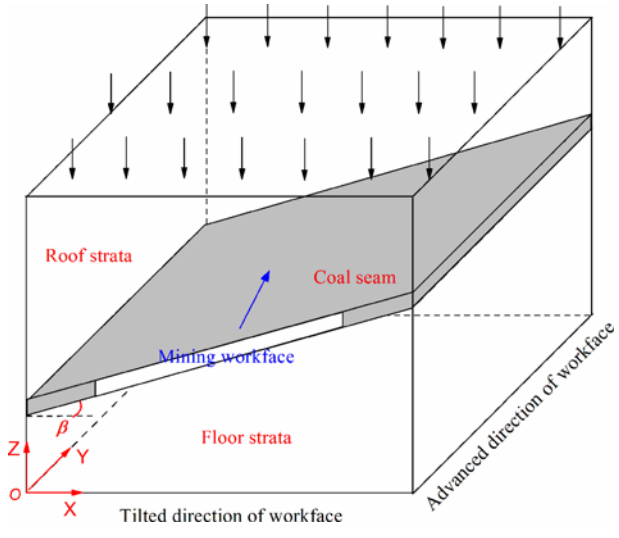

Fig. 5. Numerical Calculation Model for the Tilted Workface of Coal Seam

Table 1. Numerical Calculation Parameters for the Tilted Workface of Coal Seam

Lithology	Density / kg.m^{-3}	Bulk modulus / GPa	Tensile strength / MPa	Shear modulus / GPa	Cohesive strength / MPa	Internal friction angle / °
Roof strata	2600	3.83	1.8	2.4	4.0	40
Coal seam	1400	2.30	1.0	1.1	1.8	30
Floor strata	2645	3.43	1.5	2.0	3.5	38

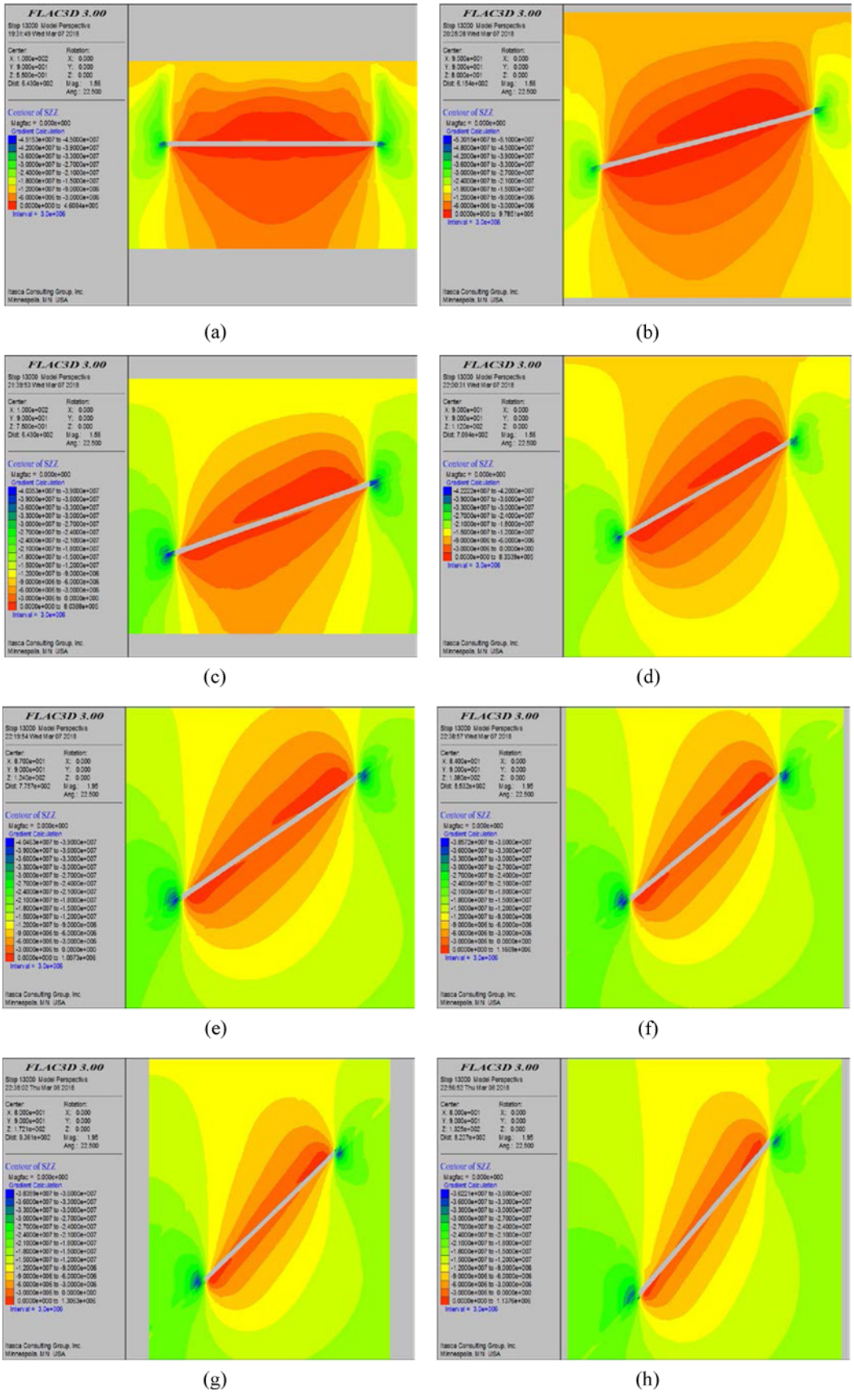

Fig. 6. Vertical Stress Contour for the Tilted Workface along the Tilted Direction with Different Dip Angles: (a) 0°, (b) 15°, (c) 20°, (d) 30°, (e) 35°, (f) 40°, (g) 45°, (h) 50°

intervals, with eight steps in total. The bottom of the model limits the displacement at the vertical direction, and the four sides (front, back, left, and right) limit the displacement at the horizontal direction. For the model, the upper surface is a free surface, and the overlying strata above roof are loaded in a uniformly distributed load to the upper surface. The numerical calculation parameters for the model are shown in Table 1. The failure criterion of the stope surrounding rock inside the model obeys to the Mohr-Coulomb yield criterion. And the Mohr-Coulomb's elastoplastic constitutive model and its yield criterion were employed in this numerical simulation (Yin *et al.*, 2019).

3.2 Vertical Stress for the Tilted Workface Floor

Figure 6 shows the workface floor's vertical stress contour along the tilted direction of coal seam in longwall mining when the dip angles are 0°, 15°, 20°, 30°, 35°, 40°, 45°, and 50°.

Figure 6 shows that the distribution law of the lateral abutment pressure of the tilted workface is similar to the horizontal workface of coal seam, but the concentration factors and their peak positions of the lateral abutment pressure on both sides of the tilted workface are no longer symmetrically distributed, as shown in Table 2. The stress concentration factor corresponds to the primary rock stress of the middle of workface in Table 2. The concentration factors of the lateral abutment pressure on both sides of the workface decrease with the increases in coal seam's dip angle, but the concentration factor of the lateral abutment pressure at the lower side of the tilted workface is always larger than that at the upper side. After mining of coal seam, a stress relaxation area is formed in workface floor strata, a stress concentration area is formed below coal body on both sides of the workface, and two areas are separated by the contour line of the primary rock stress. The vertical stress contour lines of the tilted workface floor display a "spoon-shaped" distribution form along the tilted direction of workface, and the contour lines distribution form is large on the lower side and small on the upper side. The contour lines of vertical stresses below the coal bodies on both sides of the workface display a "bubble-shaped" distribution oblique to the coal body. The obliqueness degree to the coal body increases with the increases in coal seam's dip angle. The workface floor's pressure relief degree and concentration degree of the vertical stress at both sides of the workface decrease as the normal depth of workface floor increases. The pressure relief and stress concentration scopes decrease with the increases in coal seam's dip angle, but the stress concentration degree and scope at the lower side of the tilted workface is always larger than those at the upper side.

3.3 Shearing Stress for the Tilted Workface Floor

Figure 7 shows the workface floor's shearing stress contour along the tilted direction of coal seam in longwall mining when the dip angles are 0°, 15°, 20°, 30°, 35°, 40°, 45°, and 50°.

Figure 7 shows that the "bubble-shaped" shearing stress is formed on both sides of the workface after mining, and the influential scope of shearing stress on both sides and the obliqueness degree of the upper shearing stress to the floor strata increases with the increases in coal seam's dip angle. When the dip angle is 30°, the shearing stress at the upper side of the workface floor can affect the entire areas of the workface floor. With the increases in coal seam's dip angle, the peak values of shearing stress at both sides of the workface first increase and then decrease. When the dip angle is 30° – 35°, the shearing stress reaches the maximum value. Therefore, the workface floor strata with the dip angle of 30° – 35° suffers from the most serious shear failure.

3.4 Failure Characteristics for the Tilted Workface Floor

Figure 8 shows the workface floor's plastic failure zone contour along the tilted direction of coal seam in longwall mining when the dip angles are 0°, 15°, 20°, 30°, 35°, 40°, 45°, and 50°.

Figure 8 shows that the stress in workface floor strata is relieved after mining, and a plastic failure zone covering large areas is formed. The stresses on both sides of the workface are concentrated, and two plastic failure zones are formed with certain depths and areas inside the floor strata below the coal body on both sides of the workface. The floor plastic zone's failure depth blows the lower coal body close to the failure depth inside workface floor strata. Under the lateral abutment pressure of workface, the plastic failure zone below the coal body on both sides of the workface can be connected to the plastic failure zone inside workface floor strata to form a wider plastic failure zone than workface width. The plastic failure zone inside the horizontal and the tilted workface floor along the tilted direction of

Table 2. Distribution Characteristics of the Lateral Abutment Pressure for the Tilted Workface

Buried depth / m	Workface width / m	Dip angle / °	Concentration factors of the lateral abutment pressure		Distance from peak position of the lateral abutment pressure to roadway	
			Lower side	Upper side	Lower side / m	Upper side / m
500	120	0	3.44	3.44	6.9	6.9
		15	3.40	3.39	6.4	6.7
		20	3.38	3.36	6.0	6.3
		30	3.34	3.31	5.5	5.9
		35	3.30	3.27	5.0	5.3
		40	3.26	3.23	4.5	4.8
		45	3.20	3.17	3.8	4.1
		50	3.15	3.13	3.2	3.6

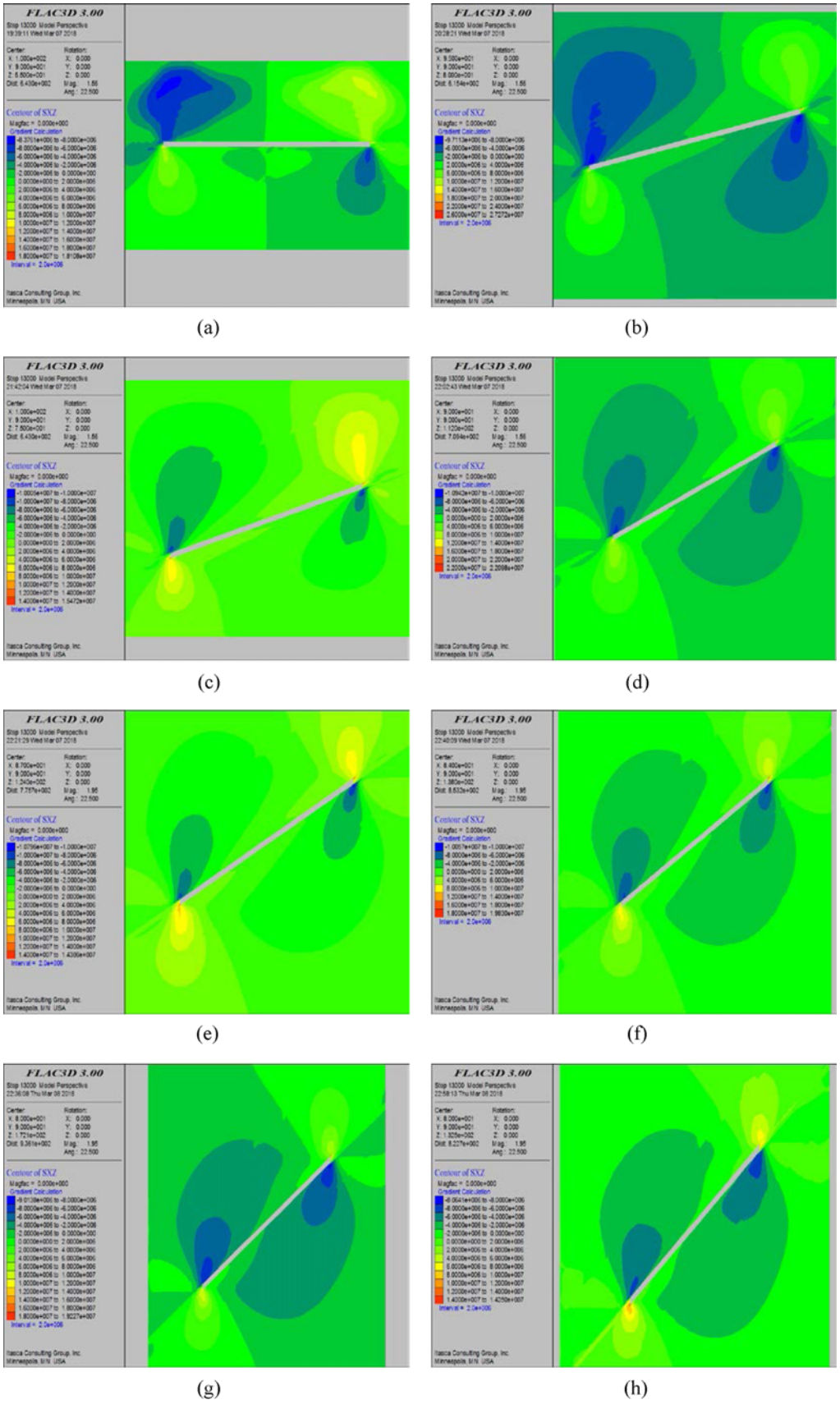

Fig. 7. Shearing Stress Contour for the Tilted Workface along the Tilted Direction with Different Dip Angles: (a) 0°, (b) 15°, (c) 20°, (d) 30°, (e) 35°, (f) 40°, (g) 45°, (h) 50°

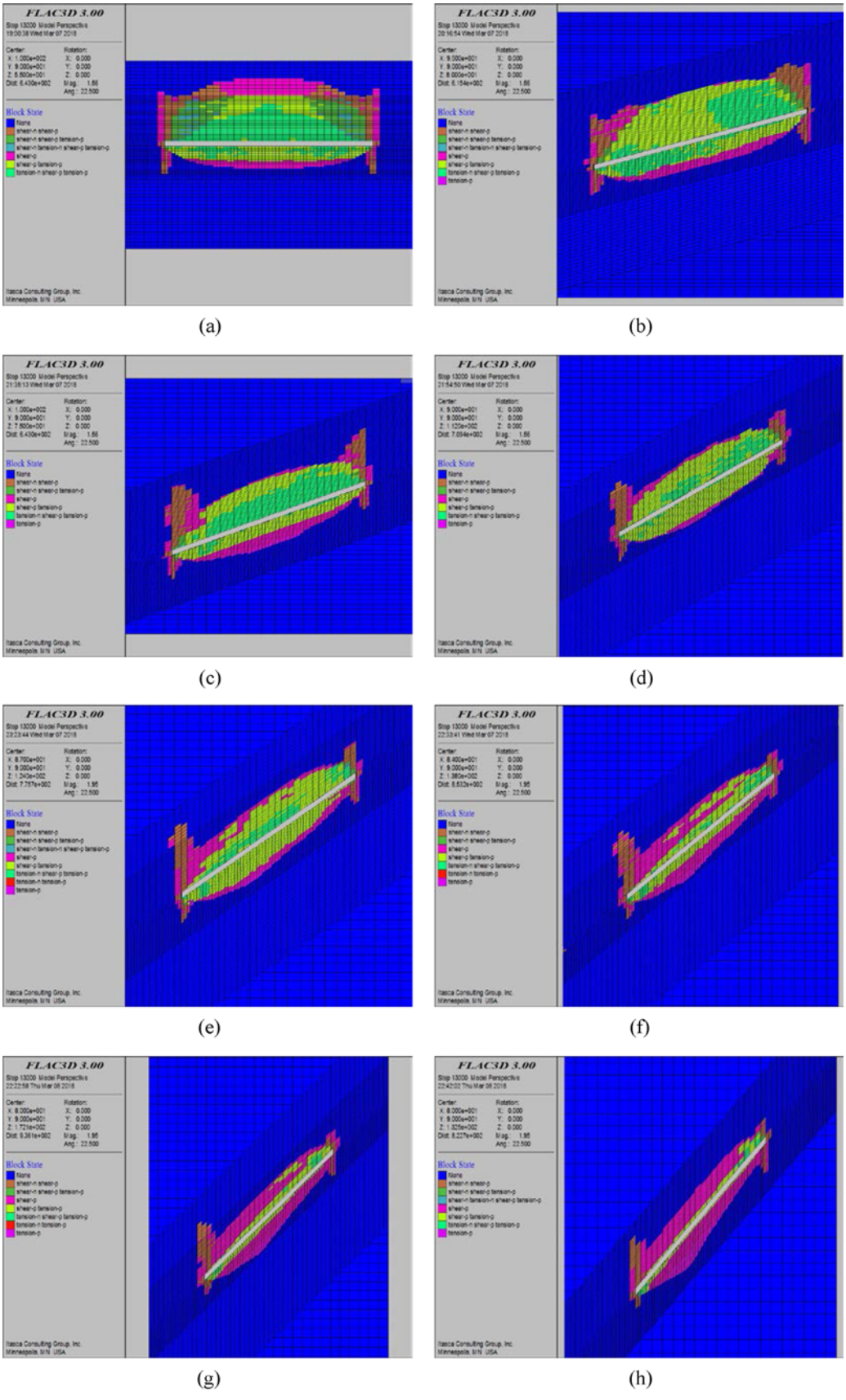

Fig. 8. Plastic Failure Zone Contour for the Tilted Workface along the Tilted Direction with Different Dip Angles: (a) 0°, (b) 15°, (c) 20°, (d) 30°, (e) 35°, (f) 40°, (g) 45°, (h) 50°

workface is symmetrically and asymmetrically distributed in "arched" and "spoon-shaped" form, respectively, which is large on the lower side of the tilted workface and small on the upper side. Otherwise, the workface floor's plastic failure depth first increases and then decreases with the increases in coal seam's dip angle. As the dip angle is 30°, the plastic failure depth inside the workface floor is the largest, while the position of the maximum plastic failure depth gradually deviates from the middle of workface toward the lower side as the coal seam's dip angle increases.

4. Effect of Workface Width on the Stress Distribution and Failure Characteristics for the Tilted Workface Floor

Simulation analysis was performed using the buried depth 500 m of coal seam and the numerical calculation parameters for the tilted workface presented in Table 1 to obtain the workface floor's vertical stress, shearing stress, and plastic failure zone in longwall mining with different dip angles (0°, 15°, 20°, 30°, 35°, 40°, 45°, and 50°) in different workface widths of 80, 120, 160, and 200 m. The details of simulated contour are not provided in this study due to space limitation.

The workface floor's vertical stress contour along the tilted direction of coal seam shows that the lateral abutment pressure's concentration factors and peak positions on both sides of the tilted workface change with the workface width and coal seam's dip angle. The change laws are described in Figs. 9 and 10. The change laws show that the concentration factors of the lateral abutment pressure on both sides of the workface decrease as coal seam's dip angle increases. However, the concentration factor of the lateral abutment pressure at the lower side of the tilted workface is always larger than that at the upper side. For different workface widths, the peak values of the lateral abutment pressure

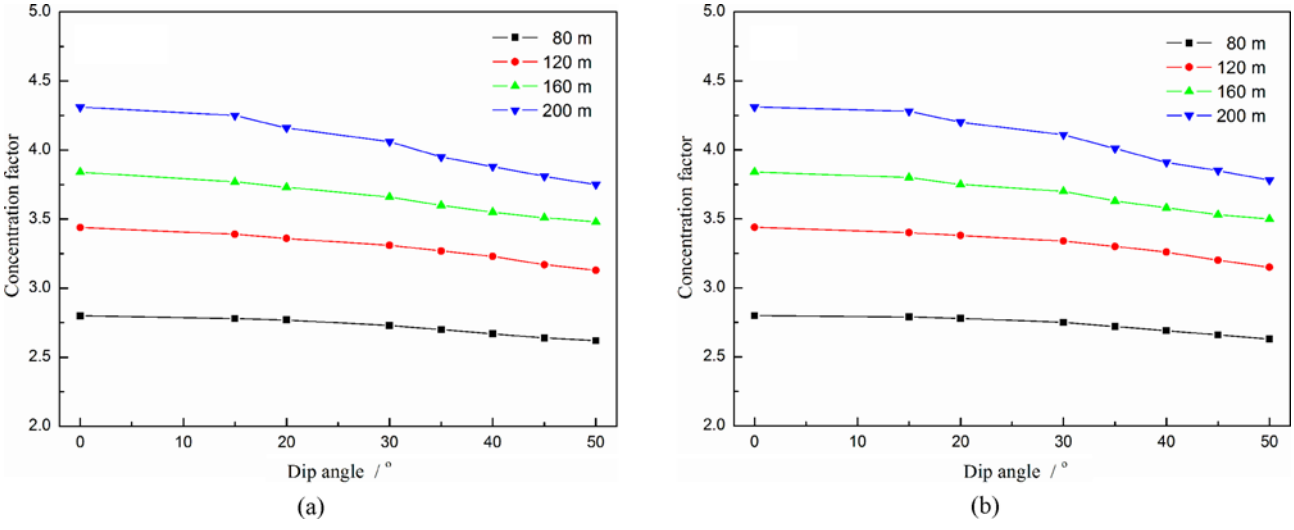

Fig. 9. Concentration Factor of the Lateral Abutment Pressure on Both Sides of the Tilted Workface: (a) Upper Side, (b) Lower Side

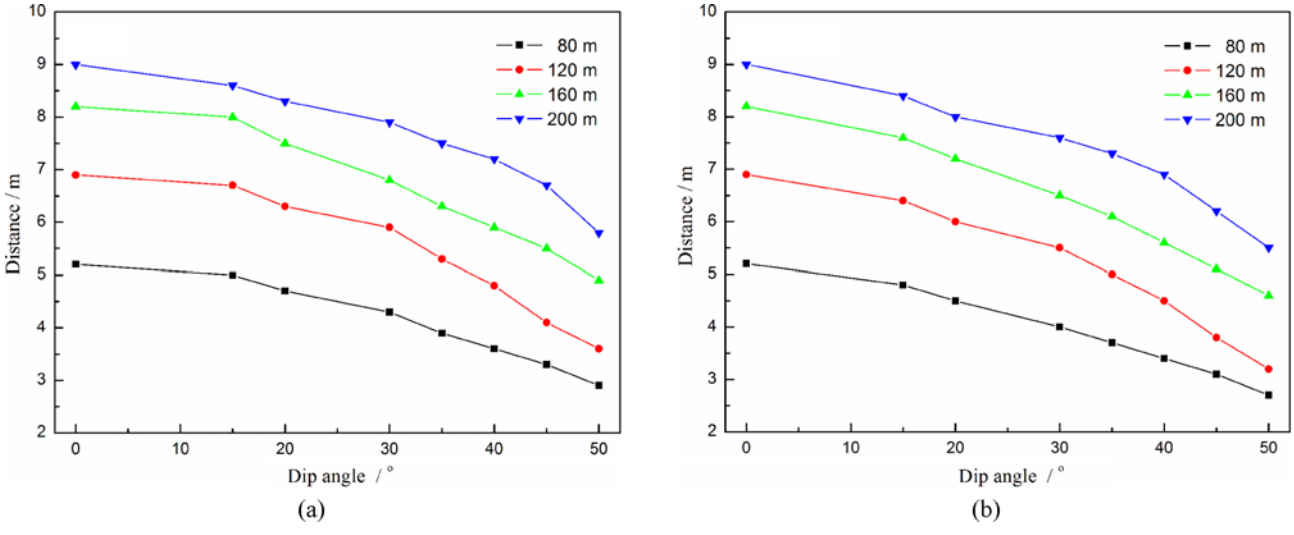

Fig. 10. Distance from Peak Position of the Lateral Abutment Pressure to the Roadway on Both Sides of the Tilted Workface: (a) Upper Side, (b) Lower Side

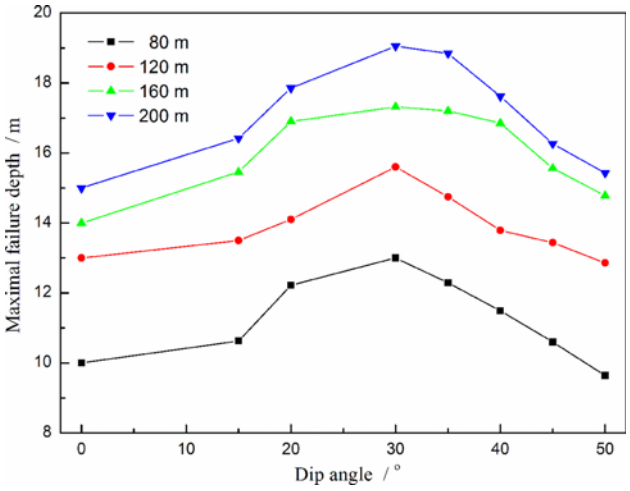

Fig. 11. Maximal Plastic Failure Depth inside the Workface Floor with the Dip Angle for Different Workface Widths

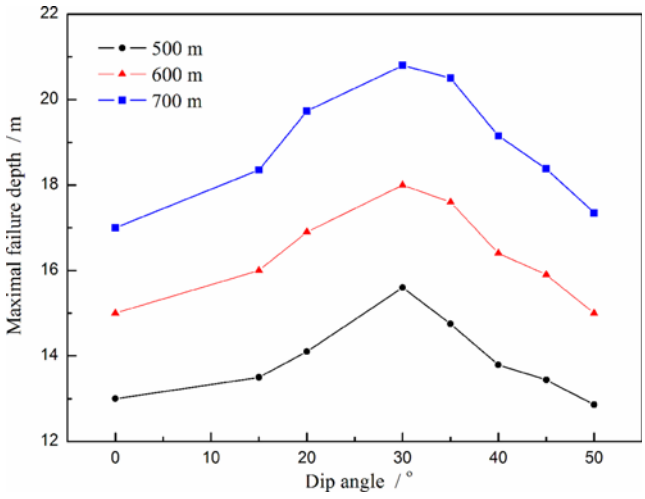

Fig. 12. Maximal Plastic Failure Depth inside the Workface Floor with the Dip Angle for Different Buried Depths

on both sides of the workface and the distance between the peak positions and the roadway decrease as the dip angle increases. For same dip angle, the concentration factors and the peak values of the lateral abutment pressure on both sides of the workface, and the distance of peak positions from the roadway increase with the increase in workface width.

The workface floor's shearing stress contour along the tilted direction of coal seam shows that the peak values of shearing stress on both sides of the workface first increase and then decrease for different workface widths. When the dip angle is 30° – 35°, the shearing stress reaches the maximum value. Thus, workface floor strata with the dip angle of 30° – 35° suffers the most serious shear failure. For same coal seam's dip angle, the peak values of shearing stress on both sides of the workface do not show significant change as workface width increases.

The plastic failure zone contour inside the workface floor along the tilted direction of coal seam shows that workface floor's plastic failure depth first increases and then decreases as the dip angle increases for different workface widths. When the dip angle is 30°, the workface floor's plastic failure depth is the largest. So workface floor strata with the dip angle of 30° – 35° suffers the most serious shearing stress and is susceptible to the shear failure. For same dip angle, the floor plastic failure depth increases with workface width, and its evolution law is described in Fig. 11.

5. Effect of Buried Depth on the Stress Distribution and Failure Characteristics for the Tilted Workface Floor

Using the coal seam's buried depth of 600 m and 700 m, and the numerical calculation parameters for the tilted workface of coal seam presented in Table 1, simulation analysis was performed on the workface floor's vertical stress, shearing stress, and plastic failure zone in longwall mining with different dip angles (0°, 15°, 20°, 30°, 35°, 40°, 45°, and 50°) in workface width of 120 m. The simulated results are compared with those at the buried depth of 500 m and workface width of 120 m. The details of the simulated contour are not provided in this study due to space limitation.

Compared with the workface floor's vertical stress contour at the buried depth of 500 m, the comparative analysis on workface floor's vertical stress, shearing stress, and plastic zone along the tilted direction of coal seam show that the workface floor's stress relief degree and range, stress concentration degree, and the influential scope on both sides of the workface increase after the buried depth increases. The lateral abutment pressure on both sides of the workface and the stress concentration factor also increase with the increases in the buried depth of coal seam. Compared with the shearing stress contour of workface floor at the buried depth of 500 m, the shearing stress on both sides of the workface increases after the buried depth increases, and reaches the maximum value when the dip angle is 30° – 35°.

The variation law between the maximal plastic failure depth inside the workface floor and the dip angle of coal seam is studied at the buried depth of 600 m, 700 m, and compared with the 500 m, the workface floor's plastic failure depth and range increase after the buried depth of coal seam increases, as shown in Fig. 12. The failure depth reaches the maximum value when the dip angle is 30°. Notably, the workface floor's plastic failure depth and range below the coal body on both sides of the workface increase after the buried depth increases and the failure depth exceeds the workface floor's maximum failure depth. Therefore, when the tilted coal seam is mined above confined aquifer, the lower area of workface floor becomes the risky areas of water inrush.

6. Conclusions

A mechanical model for the tilted workface floor along the tilted direction of coal seam in longwall mining was proposed according to the occurrence characteristics of the tilted coal

seam. According to the elasticity theory, the stress expressions of an arbitrary point inside the tilted workface floor strata were deduced. On this basis, the maximum failure depth expression for the lateral floor strata of the tilted workface was also deduced according to the Mohr–Coulomb yield criterion. Using the FLAC^{3D} software, the workface floor's stress distribution, and failure depth and shape along the tilted direction of coal seam were simulated and analyzed for different dip angles, buried depths, and workface widths of coal seam.

For different workface widths, the concentration factors of the lateral abutment pressure on both sides of the workface decrease as the dip angle increases, whereas those in the lower side of the tilted workface are always larger than those in the upper side. The peak values of the lateral abutment pressure and the distance of peak positions from the roadway on both sides of the workface decrease as the dip angle increases. For similar workface widths, the concentration factors of the lateral abutment pressure on both sides of the workface increase as the buried depth increases. For similar dip angle, the concentration factors and the peak values of the lateral abutment pressure, and the distance of peak positions from the roadway on both sides of the workface increase as the workface width increases.

After mining, a stress relaxation area is formed in workface floor strata, a stress concentration area is formed below the coal body on both sides of the workface, and two areas are separated by the contour line of the primary rock stress. The vertical stress contour lines of the tilted workface floor display "spoon-shaped" distribution form along the tilted direction of coal seam, which is large in the lower side and small in the upper side. The vertical stress contour lines below the coal bodies on both sides of the workface display the "bubble-shaped" distribution oblique to the coal body. The obliqueness degree to the coal body increases as the dip angle increases.

After mining, a "bubble-shaped" shearing stress is formed on both sides of the workface, and the influential scope of shearing stress on both sides of the workface increases as the dip angle increases. When the dip angle is 30°, the shearing stress on the upper side of the workface can affect the entire areas of workface floor. For different workface widths, the peak values of shearing stress on both sides of the workface first increase and then decrease as the dip angle increases. When the dip angle is 30°–35°, the shearing stress reaches the maximum value. For similar dip angle, the peak values of shearing stress on both sides of the workface do not show significant change as the workface width increases but increase as the buried depth of coal seam increases.

After mining, the stress relief degree and concentration degree on both sides of the workface floor decrease as the normal depth of workface floor increases. Moreover, a plastic failure zone covering large areas is formed in the workface floor, and two plastic failure zones with certain depths and areas inside the floor strata below the coal body on both sides of the workface are formed. Under the lateral abutment pressure of workface, the floor plastic failure zone below the coal body on both sides of the workface can be connected to the plastic failure zone inside the workface floor strata to form a plastic failure zone wider than workface width. Moreover, the plastic failure depth and range increase as the buried depth increases.

The plastic failure zone inside the horizontal and the tilted workface floor along the tilted direction of workface is symmetrically and asymmetrically distributed in the "arched" and "spoon-shaped" form, respectively. The workface floor's plastic failure depth first increases and then decreases as the dip angle increases. When the dip angle is 30°, the plastic failure depth inside the workface floor is the largest. For similar dip angle, the plastic failure depth inside the workface floor increases as the workface width increases. While the position of the maximum plastic failure depth gradually deviates from the middle of the workface toward the lower side as the dip angle increases.

Acknowledgements

This work was supported by the Major Research Funding Project of Natural Science of Anhui Province University (No. KJ2018ZD010), the National Natural Science Foundation of China (No. 51404013), and the Open Projects of State Key Laboratory for Geomechanics and Deep Underground Engineering at the China University of Mining and Technology (No. SKLGDUEK1212).

ORCID

Jian Sun https://orcid.org/0000-0001-9693-1077

References

Chen, J. G., Xiong, Z. Q., Li, H., Yu, Y., Nie, B. S., Wang, S. D., and Wang, X. L. (2016). "Failure characteristics of floor under predssure inclined and extra thick coal seam in full-mechanized top coal caving faces." *Chinese Journal of Rock Mechanics and Engineering*, Vol. 35, No. S1, pp. 3018-3023, DOI: 10.13722/j.cnki.jrme.2014.1450.

Cheng, Y. H., Bai, J. C., Ma, Y. K., Sun, J., Liang, Y. P., and Jiang, F. X. (2015). "Control mechanism of rock burst in the floor of roadway driven along next goaf in thick coal seam with large obliquity angle in deep well." *Shock and Vibration*, Vol. 2015, pp. 1-10, DOI: 10.1155/2015/750807.

Feng, Q. and Jiang, B. S. (2015). "Analytic solution for stress and deformation of stope floor based on integral transform." *Rock and Solid Mechanics*, Vol. 36, No. 12, pp. 3482-3487, DOI: 10.16285/j.rsm.2015.12.019.

Jiang, Y. D., Lv, Y. K., Zhao, Y. X., and Zhang, D. Y. (2011). "Similar simulation test for breakage law of working face floor in coal mining above aquifer." *Chinese Journal of Rock Mechanics and Engineering*, Vol. 30, No. 8, pp. 1571-1577.

Li, J. H., Xu, Y. C., Xie, X. F., Yao, Y. L., and Gao, Y. B. (2015). "Influence of mining height on coal seam floor failure depth." *Journal of China Coal Society*, Vol. 40, No. S2, pp. 303-310, DOI: 10.13225/j.cnki.jccs.2015.0033.

Liu, X. J., Li, X. M., and Pan, W. D. (2016). "Analysis on the floor stress distribution and roadway position in the close distance coal seams." *Arabian Journal of Geosciences*, Vol. 9, No. 2, pp. 83, DOI: 10.1007/s12517-015-2035-9.

Liu, S. L., Liu, W. T., Huo, Z. C., and Song, W. C. (2019). "Early warning information evolution characteristics of water inrush from floor in underground coal mining." *Arabian Journal of Geosciences*, Vol. 12, No. 2, p. 30, DOI: 10.1007/s12517-018-4181-3.

Liu, W. T., Liu, S. L., and Ji, B. J. (2015). "Sensitivity analysis of controlling factors on failure depth of floor based on orthogonal experiment." *Journal of China Coal Society*, Vol. 40, No. 9, pp. 1995-2001, DOI: 10.13225/j.cnki.jccs.2014.1682.

Liu, S. L., Liu, W. T., and Shen, J. J. (2017). "Stress evolution law and failure characteristics of mining floor rock mass above confined water." *KSCE Journal of Civil Engineering*, KSCE, Vol. 21, No. 7, pp. 2665-2672, DOI: 10.1007/s12205-017-1578-6.

Liu, W. T., Mu, D. R., Xie, X. X., Yang, L., and Wang, D. H. (2018). "Sensitivity analysis of the main factors controlling floor failure depth and a risk evaluation of floor water inrush for an inclined coal seam." *Mine Water and the Environment*, Vol. 37, No. 3, pp. 636-648, DOI: 10.1007/s10230-017-0497-6.

Liu, W. T., Mu, D. R., Yang, L., Li, L. Y., and Shi, C. H. (2017). "Calculation method and main factor sensitivity analysis of inclined coal floor damage depth." *Journal of China Coal Society*, Vol. 42, No. 4, pp. 849-859, DOI: 10.13225/j.cnki.jccs.2016.0863.

Lu, Y. L. and Wang, L. G. (2015). "Numerical simulation of mining-induced fracture evolution and water flow in coal seam floor above a confined aquifer." *Computers and Geotechnics*, Vol. 67, pp. 157-171, DOI: 10.1016/j.compgeo.2015.03.007.

Lu, H. F. and Yao, D. X. (2014). "Stress distribution and failure depths of layered rock mass of mining floor." *Chinese Journal of Rock Mechanics and Engineering*, Vol. 33, No. 10, pp. 2030-2039, DOI: 10.13722/j.cnki.jrme.2014.10.039.

Meng, X. R., Xu, C. H., Gao, Z. N., and Wang, X. Q. (2010). "Stress distribution and damage mechanism of mining floor." *Journal of China Coal Society*, Vol. 35, No. 11, pp. 1832-1836.

Sun, J. (2011). *Failure characteristics and water-inrush mechanism of an inclined coal seam floor,* PhD Thesis, China University of Mining and Technology, Xuzhou, China.

Sun, J. and Wang, L. G. (2014). "Instability mechanics criterion of inclined water-resisting key strata in coal seam floor." *Journal of China Coal Society*, Vol. 39, No. 11, pp. 2276-2285, DOI: 10.13225/j.cnki.jccs.2013.1354.

Sun, J., Wang, L. G., Tang, F. R., Shen, Y. F., and Gong, S. L. (2011). "Microseismic monitoring on the failure characteristics of an inclined coal seam floor." *Rock and Solid Mechanics*, Vol. 32, No. 5, pp. 1589-1595.

Tan, Y. L., Zhao, T. B., and Xiao, Y. X. (2010). "In situ investigations of failure zone of floor strata in mining close distance coal seams." *International Journal of Rock Mechanics and Mining Sciences*, Vol. 47, No. 5, pp. 865-870, DOI: 10.1016/j.ijrmms.2009.12.016.

Timoshenko, S. P. and Woinowsky-Krieger, S. W. (1959). *Theory of plates and shells*, McGraw-Hill Press, New York, USA.

Wang, L. G., Han, M., Wang, Z. S., and Ou, S. B. (2013). "Stress distribution and damage law of mining floor." *Journal of Mining and Safety Engineering*, Vol. 30, No. 3, pp. 317-322.

Xiao, F. K., Duan, L. Q., and Ge, Z. H. (2010). "Laws of floor breaking in coal mining face and gas extraction application." *Journal of China Coal Society*, Vol. 35, No. 3, pp. 417-419.

Yin, H. Y., Liliana, L., Wei, J. C., Guo, J. B., Li, Z. J., and Guan, Y. Z. (2016). "In situ dynamic monitoring of stress revolution with time and space under coal seam floor during longwall mining." *Environmental Earth Sciences*, Vol. 75, No. 18, pp. 1249, DOI: 10.1007/s12665-016-6071-x.

Yin, H. Y., Sang, S. Z., Xie, D. L., Zhao, H., Li, S. J., Li, H. S., and Zhuang, X. H. (2019). "A numerical simulation technique to study fault activation characteristics during mining between fault bundles." *Environmental Earth Sciences*, Vol. 78, No. 5, pp. 148, DOI: 10.1007/s12665-019-8142-2.

Zhang, S. C., Guo, W. J., and Li, Y. Y. (2017). "Experimental simulation of water-inrush disaster from the floor of mine and its mechanism investigation." *Arabian Journal of Geosciences*, Vol. 10, No. 22, p. 503, DOI: 10.1007/s12517-017-3287-3.

Zhang, R., Jiang, Z. Q., Li, X. H., Chao, H. D., and Sun, Q. (2013). "Study on the failure depth of thick seam floor in deep mining." *Journal of China Coal Society*, Vol. 38, No. 1, pp. 67-72.

Zhang, B. L. and Meng, Z. B. (2019). "Experimental study on floor failure of coal mining above confined water." *Arabian Journal of Geosciences*, Vol. 12, No. 4, pp. 114, DOI: 10.1007/s12517-019-4250-2.

Zhang, W., Zhang, D. S., Chen, J. B., Wang, X. F., and Xu, M. T. (2012). "Determining the optimum gateway location for extremely close coal seams." *Journal of China University of Mining and Technology*, Vol. 41, No. 2, pp. 182-188.

Zhang, J. C., Zhang, Y. Z., and Liu, T. Q. (1997). *Rock mass permeability and coal mine water inrush*, Geological Publishing House, Beijing, China.

Zhao, Q. B., Zhao, X. N., Wu, Q., Liu, C. W., and Wang, X. L. (2015). "Water burst mechanism of 'divided period and section burst' at deep coal seam floor in North China type coalfield mining area." *Journal of China Coal Society*, Vol. 40, No. 7, pp. 1601-1607, DOI: 10.13225/j.cnki.jccs.2015.0358.

Zhu, S. Y., Jiang, Z. Q., Zhou, K. J., Peng, G. Q., and Yang, C. W. (2014). "The characteristics of deformation and failure of coal seam floor due to mining in Xinmi coal field in China." *Bulletin of Engineering Geology and the Environment*, Vol. 73, No. 4, pp. 1151-1163, DOI: 10.1007/s10064-014-0612-x.